FEM-Parameterized Sensorless Vector Control of PMSM Using High-Frequency Voltage Injection

Károly Veszprémi, Gergely Szabó

FEM-parameterized Sensorless Vector Control of PMSM Using High-Frequency Voltage Injection

Gergely Szabó [1], Károly Veszprémi [2]

[1] Department of Electric Power Engineering, Budapest University of Technology and Economics Budapest, Hungary 1111, szabo.gergely@vet.bme.hu
[2] Department of Electric Power Engineering, Budapest University of Technology and Economics Budapest, Hungary 1111, veszpremi.karoly@vet.bme.hu

Abstract. The authors of the paper present the high-frequency voltage injection-based sensorless vector control method, where the test signals are injected in the estimated common coordinate system. During the modeling process a custom designed permanent magnet synchronous machine is used and its parameters are calculated using measurements combined with finite element method (FEM). The authors present an enhanced PLL-based estimator, and detail the limitations of the sensorless algorithm using the FEM results. Simulation results will be presented, where the sensorless method is combined with an incremental encoder, demonstrating the low-frequency region performance of the proposed algorithm.

Keywords: High-frequency Voltage Injection, FEM, Sensorless Vector Control, Low-frequency Performance, Incremental Encoder

1 Introduction

The injection-based vector control techniques can provide good performance in low-frequency regions, where many of the sensorless methods fail [1],[2]. Since most of the controlled electric drives involve a voltage source inverter, therefore voltage injection is an obvious choice. Based on the place of injection rotating and synchronous methods can be distinguished. The first solution adds test signals to the terminal voltages in the stationary reference frame [3],[4], while the latter one adds test signals in the estimated common coordinate system [5],[6].

In case of an actuator a usual speed-torque profile starts from standstill no-load condition, followed by a light-load speed up region and the cycle ends with a low-speed or standstill operation with high load. This common cycle covers wide range of rotational speed with various load condition. Assuming a permanent magnet synchronous machine as the rotating machine of the actuator, the implementation of a vector control algorithm requires good dynamic and precise tracking of the rotor position.

This can be achieved with a high-bandwidth and high-resolution encoder, but this could increase the system's cost. Another solution can be a cheaper encoder with additional algorithms to fulfill the requirements. The combination of high-frequency injection methods with lower cost encoders could be a reasonable alternative. In such systems in the low-frequency region the common coordinate system's angle is estimated based on the injection method, but in higher frequencies the estimation is overtaken by the physical encoder's processed signal. The design of the injection method and also the vector control algorithms require the machine parameters, which can be obtained through the combination of measurement evaluation and finite element analysis. Nevertheless, the system performance can be improved, if these methods involve the saturation characteristics of the machine, but not the static parameters.

The authors present the finite element method analysis of the used permanent synchronous motor, combined with measurement result evaluations in Section 2. This investigation's target is to obtain the machine parameters that are required for the high-frequency voltage injection method and the conventional vector control algorithm. Section 3 details the high-frequency voltage injection method including a dynamic model, used in the angle estimation. Section 4 gives an overview of the vector-controlled system with the combination of high-frequency injection and incremental encoder, including simulation results.

2 Analysis of PMSM

2.1   Finite Element Method Analysis

The presented rotating machine analysis is the combination of measurement data evaluation and finite element method (FEM). The measurements were the standard no-load and short circuit measurements at different mechanical speeds. The first one is used to calculate the pole flux Ψ_p, while the second one is used to validate the torque profile with the FEM results. Table 1 summarizes the motor parameters priory to the FEM.

Table 1. Permanent Magnet Synchronous Machine Parameters

Parameter	Value	Source
P_n	$2\ kW$	Design parameter
U_n	$330\ V$	Design parameter
I_n	$3.5\ A_{RMS}$	Nominal load measurement
n_n	$3000\ RPM$	Design parameter
R	$2.71\ \Omega$	RLC measurement
Ψ_p	$0.335\ Vs$	No-load measurement
p	2	Design parameter
J	$0.0036\ kgm^2$	Design parameter
F	$0.0011\ Nms$	Design parameter

2.2   Finite Element Method Analysis

The inputs of this analysis are the known motor topology including the applied materials. In the first step they used to calculate $d - q$ axes fluxes, which are the functions of direct-axis i_d and quadrature-axis i_q currents [7]. During the analysis the d axis was bound to the rotor's circumferential flux density distribution's positive peak.

In the first setup, the rotor is set into $\alpha_{elec} = 0°$ position, as shown in Fig. 1(a), to calculate the d axis flux $\Psi_d(i_d, i_q)$. In the second setup the rotor is positioned in $\alpha_{elec} = 90°$ direction, as shown in Fig. 1(b), in order to calculate progression of q axis flux $\Psi_q(i_d, i_q)$. For both cases all the possible $\bar{\imath} = i_d + j\,i_q$. combinations were examined on the $[-2\hat{I}_n \; 2\hat{I}_n]$ current interval with $\Delta i = 0.4A$ resolution, and the result are shown in Fig. 2(a) and (b) for the selected machine.

(a)   (b)
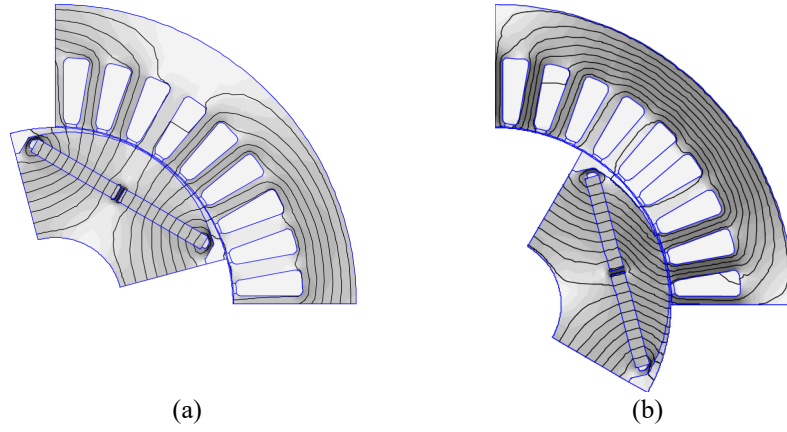
Fig. 1. Flux and inductance calculation in (a) $\alpha_{elec} = 0°$ direction alignment, (b) $\alpha_{elec} = 90°$ direction alignment

With the known progression of $\Psi_d(i_d, i_q)$ and $\Psi_q(i_d, i_q)$ fluxes the self- and cross-coupling inductances can be calculated with partial derivative or their approximation for numerical approaches as follows,

$$L_d(i_d, i_q) = \frac{\partial \Psi_d(i_d, i_q)}{\partial i_d} \approx \left. \frac{\Delta \Psi_d(i_d, i_q)}{\Delta i_d} \right|_{i_q = \text{const.}}, \tag{1}$$

$$L_{dq}(i_d, i_q) = \frac{\partial \Psi_d(i_d, i_q)}{\partial i_q} \approx \left. \frac{\Delta \Psi_d(i_d, i_q)}{\Delta i_q} \right|_{i_d = \text{const.}}, \tag{2}$$

$$L_q(i_d, i_q) = \frac{\partial \Psi_q(i_d, i_q)}{\partial i_q} \approx \left. \frac{\Delta \Psi_q(i_d, i_q)}{\Delta i_q} \right|_{i_d = \text{const.}}, \tag{3}$$
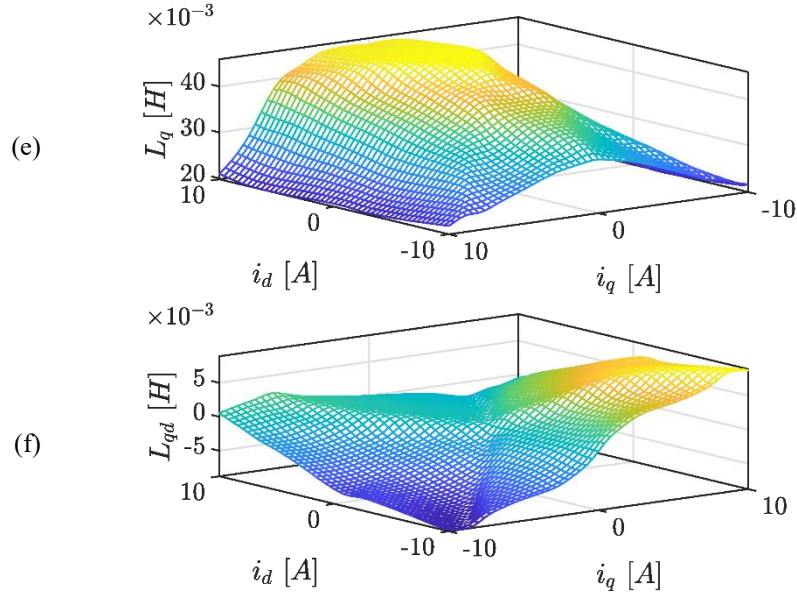
$$L_{qd}(i_d, i_q) = \frac{\partial \Psi_q(i_d, i_q)}{\partial i_d} \approx \left. \frac{\Delta \Psi_q(i_d, i_q)}{\Delta i_d} \right|_{i_q = \text{const.}}. \tag{4}$$

where L_d is the direct axis self-inductance, L_{dq} is the quadrature-to-direct axis cross-coupling inductance, L_q is the quadrature axis self-inductance and L_{qd} is the direct-to-quadrature axis cross-coupling inductance. Based on these calculations the nominal values of L_d and L_q are $15.06\ mH$ and $36.23\ mH$ respectively.
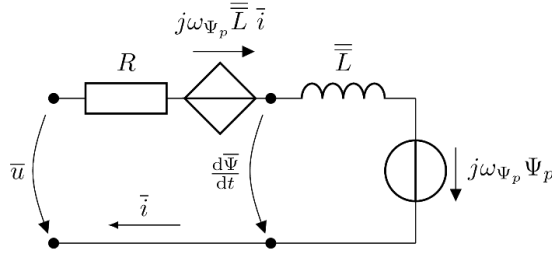
(e)

(f)
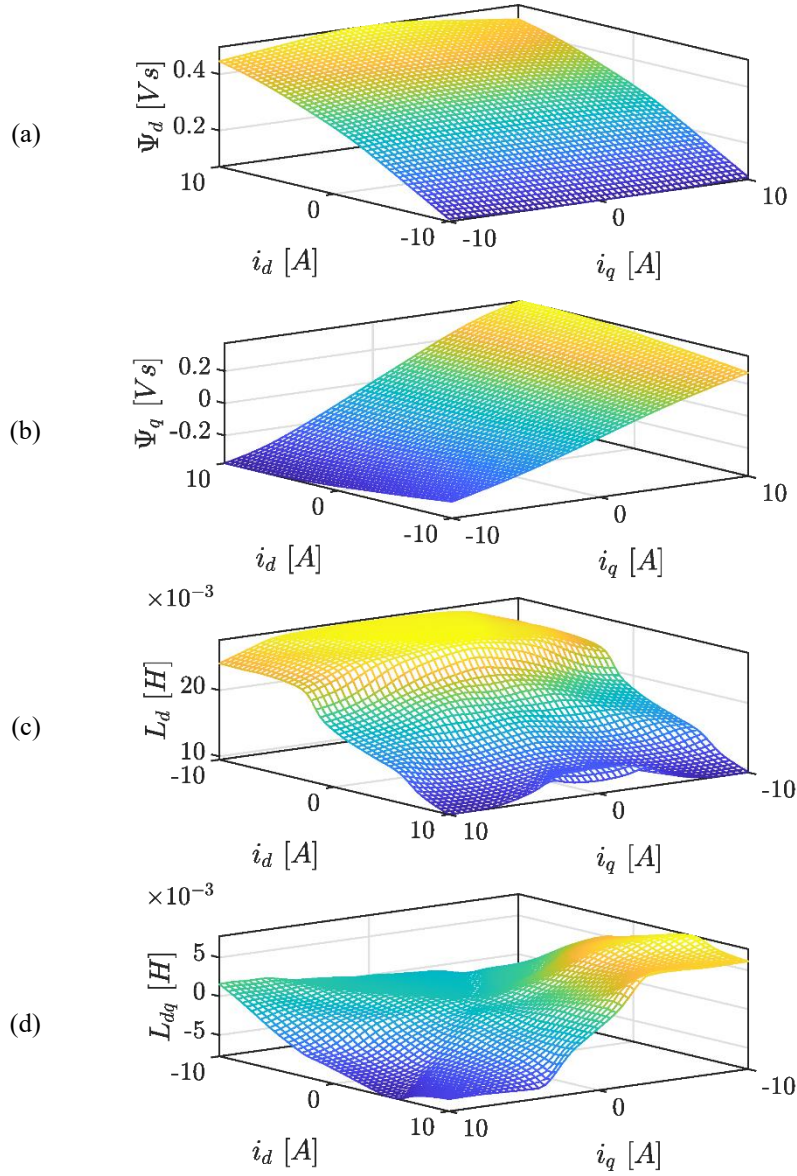
Fig. 2. Progression of fluxes and inductances

2.3   Mathematical Model of PMSM

A permanent magnet synchronous machine in $d-q$ reference frame, bound to the rotor's circumferential flux density distribution's positive peak, can be modeled as shown in Fig. 3 and with the system of differential equations in Eqs. 5- 8.

Fig. 3. Equivalent circuit of a permanent magnet synchronous machine

$$u_d = Ri_d + L_d\frac{\mathrm{d}i_d}{\mathrm{d}t} + L_{dq}\frac{\mathrm{d}i_q}{\mathrm{d}t} - \omega_{\psi_p}\left(L_{qd}i_d + L_q i_q\right), \tag{5}$$

$$u_q = Ri_q + L_q\frac{\mathrm{d}i_q}{\mathrm{d}t} + L_{qd}\frac{\mathrm{d}i_d}{\mathrm{d}t} + \omega_{\psi_p}\left(L_d i_d + L_{dq}i_q + \Psi_p\right), \tag{6}$$

$$m = \frac{3}{2}p\left((L_d - L_q)i_d i_q + \Psi_p i_q + L_{dq}i_q^2 - L_{qd}i_d^2\right), \tag{7}$$

$$(m - m_l - F\omega) = J\frac{\mathrm{d}\omega}{\mathrm{d}t}, \tag{8}$$

where u_d is the **d** axis voltage which is the real part of $\bar{u}$, R is the stator resistance, i_d is the **d** axis current which is the real part of $\bar{\imath}$, ω_{ψ_p} is the pole flux's angular speed and in Fig. 3 $\bar{\bar{L}} = \begin{bmatrix} L_d & L_{dq} \\ L_{qd} & L_q \end{bmatrix}$ and its elements are described in Eqs. 1 - 4, i_q is the q axis current which is the imaginary part of $\bar{\imath}$, u_q is the q axis voltage which is the imaginary part of $\bar{u}$, Ψ_p is the magnitude of the pole flux, m is the electromagnetic torque, J is the moment of inertia, ω is the rotor's angular speed, F is the friction loss factor, p is the number of pole pairs.
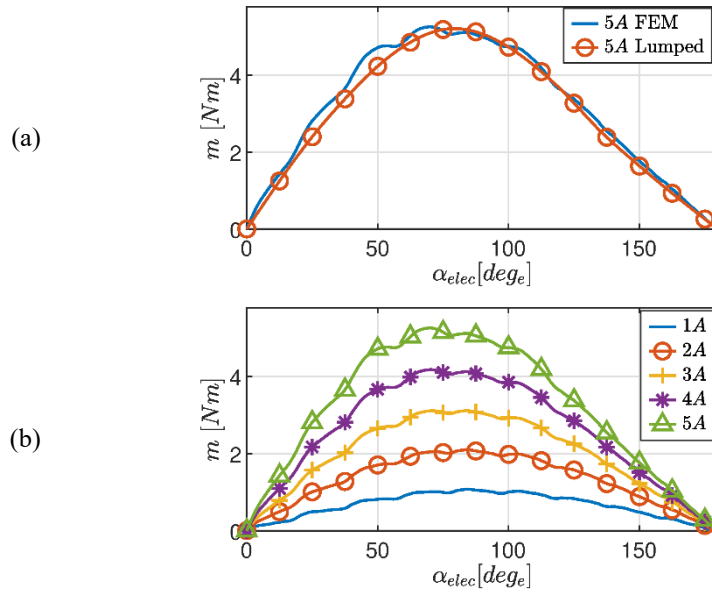
(a)

(b)

Fig. 4. (a) FEM and (b) lumped-parameter model calculated torque profiles

The machine's torque profile was calculated over one pole pitch on the $[0 \ \hat{I}_n]$ interval with $\Delta i = 1A$ and $\Delta \alpha_{elec} = 1°$ resolutions and its results are shown in Fig. 4(a). These curves were used to validate the saturating lumped-element model, by comparing the torques of each calculation methods. For $\hat{I} = 5A$ stator current vector Fig. 4(b) shows the differences between the FEM and lumped-element model's torque. The main differences between the two calculation methods, that the latter one does not include the cogging torque, but it provides reasonable accuracy and fast results.

3 High-frequency Synchronous Injection

3.1 Mathematical Model

In case of synchronous injection, high-frequency voltage signals are injected in the estimated $\hat{d} - \hat{q}$ frame, which is illustrated in Fig. 5.
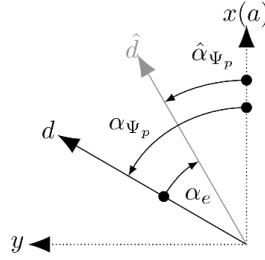
Fig. 5. Angle relations of the real d and estimated ($\hat{d}$) coordinate systems

Figure 5 also gives the angle error's definition used during the modeling process as follows,

$$\alpha_e = \alpha_{\Psi_p} - \hat{\alpha}_{\Psi_p}. \tag{9}$$

The mathematical modeling of the method was carried out using complex phasors, where complex rotating vector is bound to the sine wave. Equation 10 shows the time signals and also the corresponding complex components.

$$\begin{bmatrix} \hat{u}_{dh} \\ \hat{u}_{qh} \end{bmatrix} = \begin{bmatrix} u_h \sin(\omega_h t) \\ -u_h \cos(\omega_h t) \end{bmatrix} \Leftrightarrow \begin{bmatrix} \hat{u}_{dh} \\ \hat{u}_{qh} \end{bmatrix} = \begin{bmatrix} u_h \\ -ju_h \end{bmatrix}, \tag{10}$$

where $\hat{u}_{dh}$ and $\hat{u}_{qh}$ are the injected voltages in the estimated $\hat{d} - \hat{q}$ frame, u_h is the amplitude of the injected voltages, $\omega_h = 2\pi f_h$, where f_h is the frequency of the injected voltages, j is the imaginary unit.

Using previous definition of the angle displacement, the projections of the injected voltages on the real $d - q$ axes can be calculated as follows,

$$\begin{bmatrix} u_{dh} \\ u_{qh} \end{bmatrix} = \bar{\bar{R}}(\alpha_e) \begin{bmatrix} \hat{u}_{dh} \\ \hat{u}_{qh} \end{bmatrix}, \tag{11}$$

where $\bar{\bar{R}}$ is the rotation operator, and it can be expressed as

$$\bar{\bar{R}}(\alpha) = \begin{bmatrix} \cos(\alpha) & \sin(\alpha) \\ -\sin(\alpha) & \cos(\alpha) \end{bmatrix}. \tag{12}$$

This method requires the high-frequency current components in the stationary $x - y$ reference frame, since in a real system this is the only point where measurements can be performed. Thus, using applied voltage components, Ohm's law can be used in the form as shown in Eq. 13.

$$\begin{bmatrix} u_{dh} \\ u_{qh} \end{bmatrix} = \bar{\bar{Z}}_h \begin{bmatrix} i_{dh} \\ i_{qh} \end{bmatrix} = \bar{\bar{Z}}_h \bar{\bar{R}} \left(\alpha_{\Psi_p} \right) \begin{bmatrix} i_{xh} \\ i_{yh} \end{bmatrix},$$ **(13)**

where i_{dh} and i_{qh} are the high-frequency current components in the $d - q$ reference frame, $\bar{\bar{Z}}_h$ is the high-frequency impedance matrix that can be derived from Eqs. 5 - 8 at the injection frequency as

$$\bar{\bar{Z}}_h = \begin{bmatrix} R + j\omega_h L_d - \omega_{\Psi_p} L_{qd} & j\omega_h L_{dq} - \omega_{\Psi_p} L_q \\ j\omega_h L_{qd} + \omega_{\Psi_p} \left(L_d + \dfrac{\Psi_p}{i_d} \right) & R + j\omega_h L_q + \omega_{\Psi_p} L_{dq} \end{bmatrix} \approx \\ \begin{bmatrix} R + j\omega_h L_d & 0 \\ 0 & R + j\omega_h L_q \end{bmatrix} = \begin{bmatrix} Z_{h11} & 0 \\ 0 & \bar{Z}_{h22} \end{bmatrix}.$$ **(14)**

Equation 14 shows that some simplifications can be performed, because the anti-diagonal elements and also the $\omega_{\Psi_p} L_{qd}$ and $\omega_{\Psi_p} L_{dq}$ terms in the main-diagonal can be neglected, since their contribution to the output is much smaller than the other elements'.

Reorganizing Eq. 13, the high-frequency current components in the $x - y$ frame can be expressed as follows,

$$\begin{bmatrix} i_{xh} \\ i_{yh} \end{bmatrix} = \bar{\bar{R}}^{-1} \left(\alpha_{\Psi_p} \right) \bar{\bar{Z}}_h^{-1} \bar{\bar{R}}(\alpha_e) \begin{bmatrix} \hat{u}_{dh} \\ \hat{u}_{qh} \end{bmatrix}.$$ **(15)**

3.2 Mathematical Model

The common coordinate system's angle can be estimated with a phase-locked loop (PLL) structure, as shown in Fig. 6.
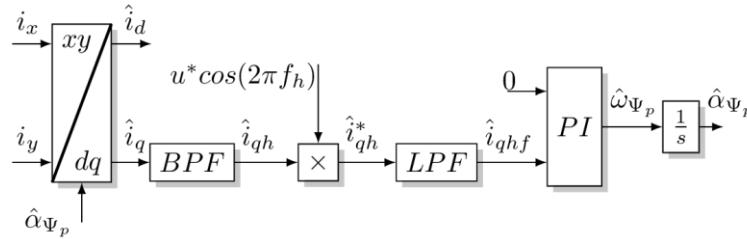

Fig. 6. Phase-locked loop

The stationary reference frame currents are transformed into the estimated common coordinate system, resulting $\hat{\imath}_d$ and $\hat{\imath}_q$ components. Thereafter, they are filtered using a band-pass filter BPF to obtain the high-frequency components $\hat{\imath}_{dh}$, $\hat{\imath}_{qh}$ and they can be modeled as

$$\hat{\imath}_{dh} = \left(\cos^2(\alpha_e)\frac{1}{\bar{Z}_{h11}} + \sin^2(\alpha_e)\frac{1}{\bar{Z}_{h22}}\right)\hat{u}_{dh}$$
$$+ \sin(\alpha_e)\cos(\alpha_e)\left(\frac{1}{\bar{Z}_{h11}} - \frac{1}{\bar{Z}_{h22}}\right)\hat{u}_{qh}, \tag{16}$$

$$\hat{\imath}_{qh} = \sin(\alpha_e)\cos(\alpha_e)\left(\frac{1}{\bar{Z}_{h11}} - \frac{1}{\bar{Z}_{h22}}\right)\hat{u}_{dh}$$
$$+ \left(\sin^2(\alpha_e)\frac{1}{\bar{Z}_{h11}} + \cos^2(\alpha_e)\frac{1}{\bar{Z}_{h22}}\right)\hat{u}_{qh}. \tag{17}$$

Equations 16 - 17 offer three solutions for the synchronous injection. In the first one both $\hat{u}_{dh}$ and $\hat{u}_{qh}$ voltages are used, often called as synchronous rotating injection. The other two solutions use only one of the available voltages, but in most of the cases $\hat{u}_{dh}$ voltage is used. In this case, which method is used in the further modeling, we are interested only in $\hat{\imath}_{qh}$, which can be reduced to the following expression,

$$\hat{\imath}_{qh} = \sin(\alpha_e)\cos(\alpha_e)\left(\frac{1}{\bar{Z}_{h11}} - \frac{1}{\bar{Z}_{h22}}\right)\hat{u}_{dh} \tag{18}$$

and its time domain equivalent is

$$\hat{\imath}_{qh}(t) = u_h \sin(\alpha_e)\cos(\alpha_e)|\bar{Y}^*|\sin(\omega_h t + \arg(\bar{Y}^*)), \tag{19}$$

where $\bar{Y}^* = \frac{1}{\bar{Z}_{h11}} - \frac{1}{\bar{Z}_{h22}}$.

In the next step $\hat{\imath}_{qh}(t)$ is fed into the phase detector part of the PLL and it is multiplied with a cosine function having the same frequency as the injected voltages and amplitude u^*, resulting $\hat{\imath}_{qh}{}^*$. Thereafter a low-pass filer LPF is applied on $\hat{\imath}_{qh}{}^*$ and its output is $\hat{\imath}_{qhf}{}^*$ which is shown in Eq. 20.

$$\hat{\imath}_{qhf}(t) = \frac{1}{2}u^* u_h \sin(\alpha_e)\cos(\alpha_e)|\bar{Y}^*|\sin(\arg(\bar{Y}^*)). \tag{20}$$

In the last step, $\hat{\imath}_{qhf}(t)$ is fed into a PI controller with zero reference, that provides an estimation for the common coordinate system's angular speed and angle. The inspection of Eq. 20 describes four possible scenarios, when the PI controller's feedback signal takes zero value, which are the following:

- u_h or u^* equals zero,
- $|\bar{Y}^*|$ becomes zero, in which case the machine is fully symmetrical in magnetic point of view,

- arc($\bar{Y}^*$) becomes zero, which is analogue to the case before,
- $\sin(\alpha_e)\cos(\alpha_e)$ becomes zero, because the angular displacement between the real and estimated coordinate systems disappears.

The second and third cases point out the limitations of the injection method, which is magnetic symmetry, when the **d** and q axes impedances are equal. This symmetry can be the result of the machine's topology, for which a good example is a surface mounted permanent magnet synchronous machine, where these impedances are equal or very close to each other even in saturated cases. On the other hand, $|\bar{Y}^*|$ and arc($\bar{Y}^*$) could become zero due to saturation effects at some combination of i_d, i_q currents.

Taking into account sensing and signal-to-noise considerations, in case of the machine-under-test the i_d, i_q combinations where the L_d / L_q ratio falls below 1.5 are considered as prohibited current pairs, where high-frequency injection cannot be applied. This region is illustrated in Fig. 7 which should be taken into account in current reference calculation. One affected algorithm is the field weakening current reference calculation, but the injection-based sensorless method is meant to operate in low-frequency regions, not in the working points above the nominal speed. Another affected algorithm is the maximum torque-per-ampere (MTPA), which is worth to implement to utilize the machine's saliency [8].
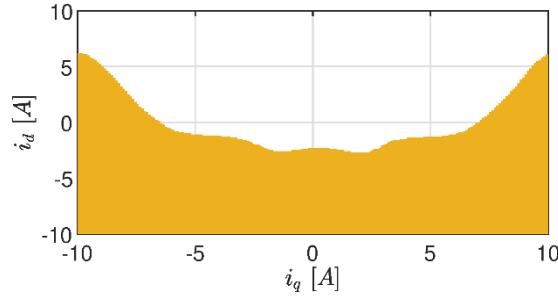
Fig. 7. Prohibited current combinations, where $L_d / L_q < 1.5$

The tuning of the PLL's PI controller can be performed using the proposed dynamic model by authors in [9] and its reduced form is shown in Fig. 8.
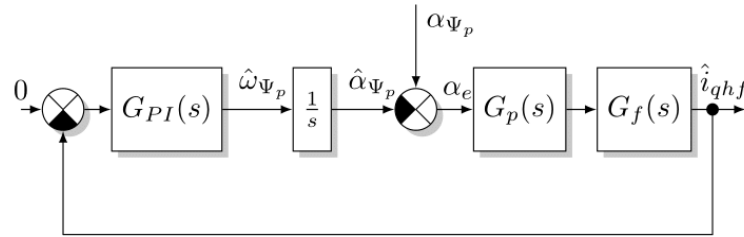
Fig. 8. Dynamic model of the PLL structure

The components of this block diagram are the following:
- $G_{PI}(s)$ is the PI controller and its transfer function is

$$G_{PI}(s) = A_p \left(1 + \frac{1}{sT_i}\right), \tag{21}$$

where A_p is the proportional gain, T_i is the integral time,
- $G_p(s)$ is process' block and its transfer function can be modeled as

$$G_p(s) = \frac{p_1 s^2 + p_2 s + p_3}{(s - \lambda_d)(s - \lambda_q)}, \tag{22}$$

where p_1, p_2, p_3 parameters are the function of the machine parameters, λ_d, λ_q are the eigenvalues of the $d-$ and $q-$ axes impedances,
- $G_f(s)$ is a low-pass filter and its transfer function is

$$G_f(s) = \frac{1}{sT_f + 1}, \tag{23}$$

where T_f is the filter's time constant.

This dynamic model offers two solutions for the PI controller's tuning. In the first approach the nominal L_d, L_q values are used and the controller is tuned to have high phase margin considering the prohibited current regions. This results a stable control in the low-frequency region, but its performance will be limited, so high dynamic changes in the common coordinate system's angle cannot be tracked. The other approach takes into account the saturation effects in the direct and quadrature axes, and constantly updates the proposed $G_p(s)$ process model. This is more complex algorithm, but it could provide better dynamics in the target application

4   Drive Simulation

Figure 9 illustrates the simulated system. The PMSM block represents the saturating, lumped-parameter machine and it was parameterized with the FEM results.
   The rotor's angular position is sensed in two ways, with an incremental encoder and with the presented high-frequency signal injection method. The final angle, $\hat{\alpha}_{\Psi_p}$ used for the coordinate transformations is obtained by the linear combination of processed incremental encoder's angle $\hat{\alpha}_{\Psi_p, inc}$ [10], and the high-frequency injection's $\hat{\alpha}_{\Psi, HF}$ estimation. The latter one dominates the low-frequency region, which is below $15\ Hz$ electrical frequency in the simulations, while the encoder's signal overtakes the estimation in high-frequency region.
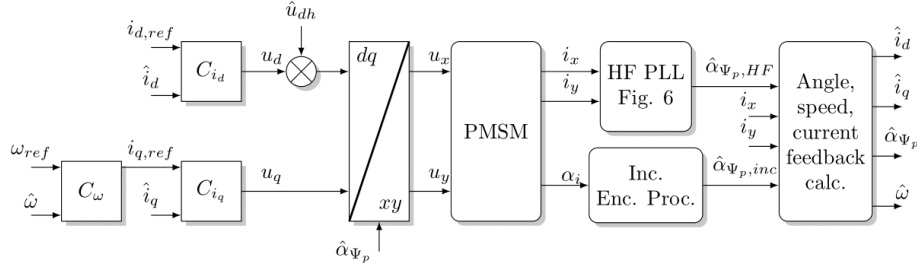
Fig. 9. Cascade control loop with the estimator

This combination of angle estimations combines both solution's advantages. In the low-frequency region with the voltage injection method rotor initial electrical position tracking and good resolution angle estimation can be achieved. On the other hand, at higher frequencies the encoder's angle provides good dynamic and precise estimation, when the high-frequency injection fails due to bad signal-to-noise ratio.

In the presented control loop all of the controllers, C_{i_d}, C_{i_q} and C_ω are PI type controllers as shown in Eq. 8. Table 3 summarizes the controller parameters [11].

Table 2. Controller parameters.

Controller	Ap	Ti
d-axis current	7.89	2.13ms
q-axis current	24.39	4.83 ms
Angular speed	0.17	79.51 ms
HF PLL	9375	28.4 ms

These parameters were obtained assuming the nominal motor parameters, and they were modified online based on the estimated saturation of the machine.

The test cycle includes all the four quadrants with applied load torque during the motoring states as shown in Fig. 10. At the end of the cycle, zero frequency performance is examined with active load torque in both directions. Figures 10(a)-(b) show the actual i_d, i_q currents and their estimations $\hat{i}_d$ and $\hat{i}_q$. Figure 10(c) shows the mechanical speed reference ω_{ref} and the actual ω_{act} shaft angular speed.

These first three figures clearly show, that this angle estimation method can be used for vector control, and stable speed-current cascade control can be achieved. At low-speed region the estimation depends on the injection method, therefore in that frequency range current ripples can be observed. As the electric speed increases, the vector control is executed using the encoder's angle, meanwhile the high-frequency signal's amplitude reaches zero.

Figure 10(d) shows the machine's torque, which is denoted as m_{act}, and the load torque, which is denoted as m_l.
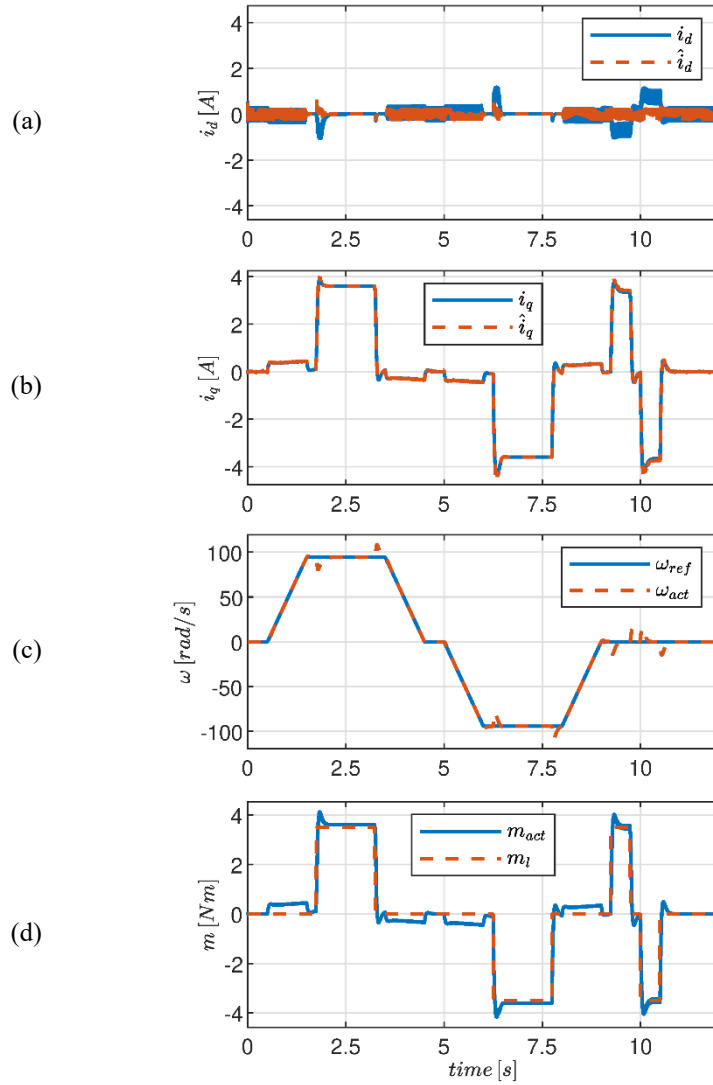
Fig. 10. Simulation results

5   Conclusion

In this paper high-frequency synchronous voltage injection was presented, and it was combined with an incremental encoder to achieve good dynamic vector control on the whole frequency range.

The machine parameters were calculated using finite element method and measurement results evaluation. The analytical results and mathematical description of the injection method were presented, based on the comprehensive FEM analysis, a

novel prohibited range is defined for the high-frequency injection method. The angle estimation was performed with a PLL structure, for which new dynamic structure was proposed, which can be used for its PI controller tuning. The FEM results can also be involved in this dynamic model, since it depends on the machine parameters.

References

1. X. Lin, W. Huang, and W. Jiang, "Position sensorless direct torque control for pmsm based on pulse high frequency stator flux injection at low speed," in 2019 IEEE 28th International Symposium on Industrial Electronics (ISIE), 2019, pp. 366–371
2. S. Medjmadj, D. Diallo, C. Delpha, and G. Yao, "A salient-pole pmsm position and speed estimation at standstill and low speed by a simplified hf injection method," in IECON 2017 - 43rd Annual Conference of the IEEE Industrial Electronics Society, 2017, pp. 8317–8322.
3. J. M. Liu and Z. Q. Zhu, "Sensorless control strategy by squarewaveform high-frequency pulsating signal injection into stationary reference frame," IEEE Journal of Emerging and Selected Topics in Power Electronics, vol. 2, no. 2, pp. 171–180, June 2014.
4. G. Wang, D. Xiao, G. Zhang, C. Li, X. Zhang, and D. Xu, "Sensorless control scheme of ipmsms using hf orthogonal square-wave voltage injection into a stationary reference frame," IEEE Transactions on Power Electronics, vol. 34, no. 3, pp. 2573–2584, 2019.
5. Ji-Hoon Jang, Seung-Ki Sul, Jung-Ik Ha, K. Ide, and M. Sawamura, "Sensorless drive of surface-mounted permanent-magnet motor by high frequency signal injection based on magnetic saliency," IEEE Transactions on Industry Applications, vol. 39, no. 4, pp. 1031–1039, July 2003.
6. S. Kim, J. Ha, and S. Sul, "Pwm switching frequency signal injection sensorless method in ipmsm," IEEE Transactions on Industry Applications, vol. 48, no. 5, pp. 1576–1587, Sep. 2012.
7. B. Stumberger, G. Stumberger, D. Dolinar, A. Hamler, and M. Trlep, "Evaluation of saturation and cross-magnetization effects in interior permanent-magnet synchronous motor," IEEE Transactions on Industry Applications, vol. 39, no. 5, pp. 1264–1271, 2003.
8. H. Kim, Y. Lee, S. Sul, J. Yu, and J. Oh, "Online mtpa control of ipmsm based on robust numerical optimization technique," IEEE Transactions on Industry Applications, vol. 55, no. 4, pp. 3736–3746, 2019.
9. G. Szabó and K. Veszprémi, "Sensorless vector control of permanent magnet synchronous machine using high-frequency signal injection," Acta Polytechnica Hungarica, vol. 17, no. 4, pp. 145–163, 2020.
10. A. F. Ilmiawan, D. Wijanarko, A. H. Arofat, H. Hindersyah, and A. Purwadi, "An easy speed measurement for incremental rotary encoder using multi stage moving average method," in 2014 International Conference on Electrical Engineering and Computer Science (ICEECS), 2014, pp. 363–368.
11. L. Wang, S. Chai, D. Yoo, L. Gan, and K. Ng, PID and predictive control of electrical drives and power converters using MATLAB/Simulink. John Wiley & Sons, 2015.